

TOI-132 b: A short-period planet in the Neptune desert transiting a V = 11.3 G-type star

Matías R. Díaz, James S. Jenkins, Davide Gandolfi, Eric D. Lopez, Maritza G. Soto, Pía Cortés-Zuleta, Zaira M. Berdiñas, Keivan G. Stassun, Karen A. Collins, José I. Vines, et al.

▶ **To cite this version:**

Matías R. Díaz, James S. Jenkins, Davide Gandolfi, Eric D. Lopez, Maritza G. Soto, et al.. TOI-132 b: A short-period planet in the Neptune desert transiting a V = 11.3 G-type star . Monthly Notices of the Royal Astronomical Society, 2020, 493, pp.973-985. 10.1093/mnras/staa277 . insu-03667118

HAL Id: insu-03667118
https://insu.hal.science/insu-03667118

Submitted on 13 May 2022

HAL is a multi-disciplinary open access archive for the deposit and dissemination of scientific research documents, whether they are published or not. The documents may come from teaching and research institutions in France or abroad, or from public or private research centers.

L'archive ouverte pluridisciplinaire **HAL**, est destinée au dépôt et à la diffusion de documents scientifiques de niveau recherche, publiés ou non, émanant des établissements d'enseignement et de recherche français ou étrangers, des laboratoires publics ou privés.

Monthly Notices
of the
ROYAL ASTRONOMICAL SOCIETY

MNRAS **493,** 973–985 (2020)
Advance Access publication 2020 January 29

doi:10.1093/mnras/staa277

TOI-132 b: A short-period planet in the Neptune desert transiting a $V = 11.3$ G-type star*

Matías R. Díaz [1]†, James S. Jenkins [1]†, Davide Gandolfi,[2] Eric D. Lopez,[3] Maritza G. Soto,[4] Pía Cortés-Zuleta,[1] Zaira M. Berdiñas,[1] Keivan G. Stassun [5,6], Karen A. Collins,[7] José I. Vines,[1] Carl Ziegler [8], Malcom Fridlund,[9,10] Eric L. N. Jensen,[11] Felipe Murgas,[12,13] Alexandre Santerne [14], Paul A. Wilson [15,16], Massimiliano Esposito,[17] Artie P. Hatzes,[17] Marshall C. Johnson [18], Kristine W. F. Lam,[19] John H. Livingston [20], Vincent Van Eylen,[21,22] Norio Narita,[12,23,24,25] Cesar Briceño,[26] Kevin I. Collins,[27] Szilárd Csizmadia [28], Michael Fausnaugh,[29] Tianjun Gan,[30] Rafael A. García,[31,32] Iska Georgieva,[9] Ana Glidden,[29,33] Lucía González-Cuesta,[12,13] Jon M. Jenkins,[34] David W. Latham,[7] Nicholas M. Law,[35] Andrew W. Mann,[35] Savita Mathur,[12,13] Ismael Mireles,[29] Robert Morris,[34,36] Enric Pallé,[12,13] Carina M. Persson,[9] George Ricker,[29] Stephen Rinehart,[3] Mark E. Rose,[34] Sara Seager,[29,33,37] Jeffrey C. Smith,[34,36] Thiam-Guan Tan,[38] Andrei Tokovinin [26], Andrew Vanderburg,[39] Roland Vanderspek,[29] Joshua N. Winn[22] and Daniel A. Yahalomi[7]

Affiliations are listed at the end of the paper

Accepted 2020 January 17. Received 2020 January 8; in original form 2019 November 4

ABSTRACT

The Neptune desert is a feature seen in the radius-period plane, whereby a notable dearth of short period, Neptune-like planets is found. Here, we report the Transiting Exoplanet Survey Satellite (*TESS*) discovery of a new short-period planet in the Neptune desert, orbiting the G-type dwarf TYC 8003-1117-1 (TOI-132). *TESS* photometry shows transit-like dips at the level of ∼1400 ppm occurring every ∼2.11 d. High-precision radial velocity follow-up with High Accuracy Radial Velocity Planet Searcher confirmed the planetary nature of the transit signal and provided a semi-amplitude radial velocity variation of $11.38\ ^{+0.84}_{-0.85}$ m s^{-1}, which, when combined with the stellar mass of 0.97 ± 0.06 M$_\odot$, provides a planetary mass of $22.40^{+1.90}_{-1.92}\,M_\oplus$. Modelling the *TESS* light curve returns a planet radius of $3.42^{+0.13}_{-0.14}\,R_\oplus$, and therefore the planet bulk density is found to be $3.08^{+0.44}_{-0.46}$ g cm^{-3}. Planet structure models suggest that the bulk of the planet mass is in the form of a rocky core, with an atmospheric mass fraction of $4.3^{+1.2}_{-2.3}$ per cent. TOI-132 b is a *TESS* Level 1 Science Requirement candidate, and therefore priority follow-up will allow the search for additional planets in the system, whilst helping to constrain low-mass planet formation and evolution models, particularly valuable for better understanding of the Neptune desert.

Key words: techniques: photometric – techniques: radial velocities – planets and satellites: fundamental parameters – planetary systems.

1 INTRODUCTION

The *Kepler* space telescope (Borucki 2010) has allowed us to understand the population of small planets ($R_p < 4\,R_\oplus$) in a

* Based on observations made with the ESO-3.6m telescope at La Silla Observatory (Chile) under programs 0103.C-0442 and 1102.C-0923.

† E-mail: matias.diaz.m@ug.uchile.cl (MRD); jjenkins@das.uchile.cl (JSJ)

© 2020 The Author(s)
Published by Oxford University Press on behalf of the Royal Astronomical Society

Downloaded from https://academic.oup.com/mnras/article/493/1/973/5717324 by guest on 13 May 2022

real statistical sense for the first time. *Kepler* revealed that the majority of planets are the so-called super-Earths, with an occurrence rate of ∼6 per cent of Earth-size planets around Sun-like stars (Petigura, Howard & Marcy 2013). *Kepler* has also unveiled a bimodality in the radius distribution of such planets (Fulton et al. 2017; Van Eylen et al. 2018), which could be the result of photoevaporation of the planetary atmosphere due to the intense stellar radiation (Lopez & Fortney 2013; Owen & Wu 2013; Jin et al. 2014; Chen & Rogers 2016). Furthermore, planets in the Neptune regime are also more abundant than the large gas giant planets. It is important to note that the distinction between super-Earths and sub-Neptunes is based on the radius, where the first class is commonly defined as planets with $1\,R_\oplus < R_\mathrm{p} < 2\,R_\oplus$, while the latter comprises planets with $2\,R_\oplus < R_\mathrm{p} < 4\,R_\oplus$. From *Kepler* statistics, 25 per cent of Sun-like stars in our Galaxy is found to host at least one small planet ($R_\mathrm{p} < 4\,R_\oplus$) on a short period orbit ($P < 100$ d; Batalha et al. 2013; Marcy et al. 2014).

Although Neptune-sized planets orbiting Sun-like stars are fairly abundant (e.g. Espinoza et al. 2016; Luque et al. 2019; Mayo et al. 2019; Palle et al. 2019), at short orbital periods they are very rare. A number of early studies indicated a lack of Neptune-sized planets with periods shorter than 2–4 d (Benítez-Llambay, Masset & Beaugé 2011; Szabó & Kiss 2011; Beaugé & Nesvorný 2013; Helled, Lozovsky & Zucker 2016), and the term 'Neptune desert' was coined to explain this paucity. Mazeh, Holczer & Faigler (2016) placed this dearth on a statistical footing, whilst providing robust boundaries for the region. Even though the dominant mechanism that produces this desert is currently unknown, models that invoke tidal disruption of a high-eccentricity migration planet, coupled with photoevaporation can explain the triangular shape of the gap described by Mazeh et al. (2016; see also Lundkvist et al. 2016; Owen & Lai 2018).

The Neptune desert may be a region of parameter space with a paucity of such planets, but it is not completely empty. West et al. (2019) discovered the planet NGTS-4*b* as part of the Next Generation Transit Survey (Wheatley et al. 2018). Although the star is fairly faint ($V = 13.14$), making the constraints on the radius and mass difficult, the planet resides inside the boundaries of the desert, as defined by Mazeh et al. (2016). A more recent example was found using data from the Transiting Exoplanet Survey Satellite (*TESS*; Ricker et al. 2015): a planet orbiting the star HD 21966 residing in the edge of this region (Esposito et al. 2019). The primary goal of *TESS* is to discover 50 planets with radii $\leq 4\,R_\oplus$ transiting stars brighter than V $\leq$ 12, for which precise masses can be measured using high-precision Doppler spectroscopy, better constraining the planetary bulk density. In doing so, the mission is also providing unprecedented targets to follow-up to study the Neptune desert, particularly the discovery of the first ultrahot Neptune, LTT 9779 b ($R_\mathrm{p} = 4.59 \pm 0.23\,R_\oplus$, $P = 0.79$ d; Jenkins et al. 2020). This planet resides on the edge of the Neptune desert, and since the star is bright ($V = 9.76$), detailed follow-up can be performed to shed light on the processes that sculpt the desert. However, more such examples are necessary in order to uncover the dominant process(es) at play.

Here, we present the discovery of TOI-132 b, a 22.4-$M_\oplus$ Neptune-sized planet discovered by *TESS* and confirmed using high-precision Doppler spectroscopy from the High Accuracy Radial velocity Planet Searcher (HARPS; Pepe et al. 2002) and additional ground-based transit detections.

2 PHOTOMETRY

2.1 *TESS* photometry

TYC 8003-1117-1 (also known as TIC 89020549, TOI-132) was observed by *TESS* in Sector 1 on Camera 2 in short-cadence mode ($T_\mathrm{exp} = 2$ min). The total time baseline of the observations is 27.87 d, spanning from 2018 July 25 to August 22. TOI-132.01 was identified as a potential transiting planet signature by the Science Processing Operations Center (SPOC) in the transit search run on Sector 1 (Jenkins 2002; Jenkins et al. 2010) and promoted to TOI status by the *TESS* Science Office based on the SPOC Data Validation (DV) reports (Twicken et al. 2018; Li et al. 2019).

The target was selected from the *TESS* alerts website,[1] based on the magnitude of the star ($V = 11.2$ mag) and period of the candidate, since it presented a good opportunity to be confirmed relatively quickly with HARPS. In addition, from the DV report for TOI-132.01, we note the planetary signature passed all of the diagnostic tests conducted by DV, including the odd/even depth test, the weak secondary test, the ghost diagnostic test, and the difference image centroid shift test.

We retrieved the photometry provided by the *TESS* SPOC pipeline (Jenkins et al. 2016), and accessed the data from the simple aperture photometry (`SAP_FLUX`) and the Presearch Data Conditioning simple aperture photometry (`PDCSAP_FLUX`, Smith et al. 2012; Stumpe et al. 2014), which contains systematics-corrected data using the algorithms previously used for *Kepler* (Jenkins 2017). The median-normalized `SAP_FLUX` photometry is shown in the top panel of Fig. 1. Bottom panel shows the `PDCSAP_FLUX` photometry, divided by its median value and after applying a 4σ clipping rejection with the transits masked out. This light curve is used throughout all the analyses in this paper. The gap in the middle of the time series occurred when the observations were stopped to allow for the data down-link. Finally, in order to avoid any bias in our analysis, we excluded the photometric measurements between (BJD - 2457000) 1347.5 and 1349.3 (the grey-shaded area) given that the spacecraft pointing jitter was higher than nominal, as described by Huang et al. (2018) and also noted in recent *TESS* discoveries (see e.g. Espinoza et al. 2019b). A total of 11 transit events were considered for further analysis in this work. Magnitudes and stellar parameters for TOI-132 are shown in Table 1 (see also Section 4).

We also performed a time–frequency analysis (Mathur et al. 2010) and computed the autocorrelation function for the *TESS* light curve to look for signatures of rotation modulation following the methodology described in García et al. (2014), Ceillier et al. (2017) and Santos et al. (2019). However, no significant signal was found. The length of the data is too short to find a periodicity larger than 9 d as we require to observe at least three periods.

2.2 Ground-based time series photometry

We acquired ground-based time series follow-up photometry of TOI-132 as part of the *TESS* Follow-up Observing Program to attempt to rule out nearby eclipsing binaries (NEBs) in all stars that could be blended in the *TESS* aperture as potential sources of the *TESS* detection. Furthermore, we attempt to (i) detect the transit-like event on target to confirm the event depth and thus the *TESS* photometric deblending factor, (ii) refine the *TESS* ephemeris, (iii)

[1] //https://tev.mit.edu/data/

Downloaded from https://academic.oup.com/mnras/article/493/1/973/5717324 by guest on 13 May 2022

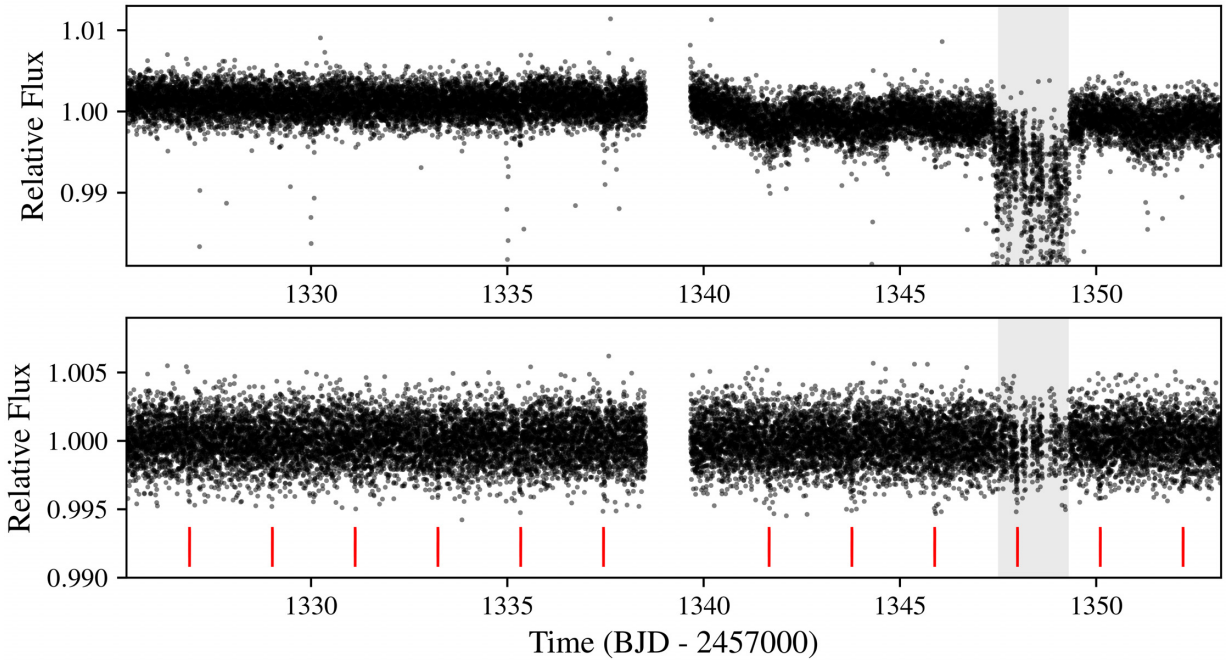


Figure 1. *TESS* light curve for TOI-132. Top panel shows the Simple Aperture Photometry (SAP_FLUX). Bottom panel shows the systematic-corrected PDCSAP_FLUX photometry after normalizing by the median and rejecting 4σ values. The red vertical lines show the position of the 12 transits identified in the *TESS* alert from Sector 1. The grey-shaded area highlights the photometric measurements removed from the analysis due to an increase in the spacecraft pointing jitter.

provide additional epochs of transit centre time measurements to supplement the transit timing variation (TTV) analysis, and (iv) place constraints on transit depth differences across filter bands. We used the `TESS Transit Finder`, which is a customized version of the `Tapir` software package (Jensen 2013), to schedule our transit observations.

We observed TOI-132 continuously for 443 min on UTC 2018 September 9 in R_c band ($\sigma \sim 1.8$ mmag) from the Perth Exoplanet Survey Telescope near Perth, Australia. The 0.3-m telescope is equipped with a 1530 × 1020 pixels SBIG ST-8XME camera with an image scale of $1\farcs2$ pixel^{-1} resulting in a 31 arcmin × 21 arcmin field of view. A custom pipeline was used to calibrate the images and extract the differential photometry using an aperture with radius $8\farcs2$. The images have typical stellar point spread functions (PSFs) with a full width at half-maximum (FWHM) of ∼4 arcsec. The data rule out NEBs in stars within $2\farcs5$ of the target star that are fainter by as much as 6.4 magnitudes in R_c band.

We also observed full predicted transit durations of TOI-132 continuously in z-short band on UTC 2018 November 14, UTC 2019 June 19, and UTC 2019 July 6 from the Las Cumbres Observatory Global Telescope (LCOGT) 1.0 m telescopes (Brown et al. 2013) at Cerro Tololo Inter-American Observatory for 277, 335, and 283 min, respectively. Another full transit was observed continuously for 232 min in B band on UTC 2019 August 2 from an LCOGT 1.0 m telescope at Siding Spring Observatory. The 4096 × 4096 LCOGT SINISTRO cameras have an image scale of $0\farcs389$ pixel^{-1} resulting in a 26 arcmin × 26 arcmin field of view. The images were calibrated by the standard LCOGT BANZAI pipeline (McCully et al. 2018) and the photometric data were extracted using the `AstroImageJ` (`AIJ`) software package (Collins et al. 2017), yielding a mean error of 800 ppm for the z-short band data we include in our analysis.

The November data rule out NEBs in all stars within $2\farcs5$ of the target star that are fainter by as much as 8.7 mag in z-short band, which includes all known *Gaia* DR2 stars that are blended in the *TESS* aperture. The June observation confirmed a ∼1400 ppm deep ingress on target arriving ∼80 min late relative to the original TOI ephemeris. The follow-up ephemeris was adjusted to account for the 80 min offset. The July observation confirmed an on-time arrival of a ∼1400 ppm deep full transit relative to the adjusted ephemeris, indicating that the transit timing is consistent with a linear ephemeris. The images have stellar PSF FWHMs of $\sim2\farcs0$, and the transit signal is reliably detected on target using a follow-up aperture with radius as small as $1\farcs5$. Therefore, the aperture is negligibly contaminated by the nearest *Gaia* neighbor $10\farcs5$ south. Systematic effects start to dominate the light curve for smaller apertures. The August B-band observation confirmed an on-time arrival of a ∼1400 ppm deep full transit, indicating that the transit-like event does not show a filter-dependent depth in B and z-short bands, which photometrically strengthens the case for a transiting exoplanet orbiting around TOI-132.

3 HARPS SPECTROSCOPIC FOLLOW-UP

TOI-132 was observed using HARPS (Pepe et al. 2002) spectrograph mounted at the 3.6-m ESO telescope at La Silla observatory, during seven consecutive nights between 2019 April 2 and 9, as part of the observing program 0103.C-0442. The exposure time was set to 1200–1800 s, which allowed us to achieve a mean signal-to-noise (S/N) ratio of ∼35 pixel^{-1} at 5500 Å in the extracted spectra giving rise to a typical error of ∼1.9 m s^{-1}. Upon examination of the radial velocities (RVs) and after performing a one-planet model fit to the *TESS* period, we found it necessary to acquire more observations to improve the phase coverage. Therefore, 13 additional RVs were

Downloaded from https://academic.oup.com/mnras/article/493/1/973/5717324 by guest on 13 May 2022

Table 1. Stellar parameters for TOI-132.

Parameter	Value	Source
TESS Names	TIC89020549 (TOI-132.01)	
RA (hh:mm:ss)	22:33:35.8683	*Gaia*
Dec. (dd:mm:ss)	−43:26:11.9167	*Gaia*
μ RA (mas yr^{-1})	35.553 ± 0.043	*Gaia*
μ (mas yr^{-1})	− 53.055 ± 0.054	*Gaia*
Parallax (mas)	6.08 ± 0.04	*Gaia**
Distance (pc)	164.47 ± 27.32	*Gaia*
SpT	G8V	This work
Photometry		
B_T	12.07 ± 0.17	Tycho-2
V_T	11.29 ± 0.07	Tycho-2
g	11.85 ± 0.02	APASS
r	11.24 ± 0.01	APASS
i	11.08 ± 0.02	APASS
TESS	10.80 ± 0.02	Stassun et al. (2018b)
Gaia	11.2935 ± 0.0003	*Gaia*
J	10.14 ± 0.02	2MASS
H	9.76 ± 0.02	2MASS
K_s	9.65 ± 0.02	2MASS
W_1	9.61 ± 0.02	WISE
W_2	9.69 ± 0.02	WISE
W_3	9.60 ± 0.04	WISE
W_4	8.72 ± 0.42	WISE
Derived parameters		
$T_{\rm eff}$ (K)	5397 ± 46	This work
log g (cm s^{-2})	4.48 ± 0.23	This work
[Fe/H] (dex)	0.16 ± 0.10	This work
L (L$_\odot$)	0.60 ± 0.05	This work
R (R$_\odot$)	0.90 ± 0.02	This work
M (M$_\odot$)	0.97 ± 0.06	This work
$v\ sin(i)$ (km s^{-1})	3.00 ± 0.30	This work
$v_{\rm mac}$ (km s^{-1})	1.74 ± 0.20	This work
$\rho_\star$ (g cm^{-3})	1.89 ± 0.15	This work
log R_{HK} (dex)	− 5.02 ± 0.13	This work
Age (Gyr)	$6.34^{+0.42}_{-2.35}$	This work
(U,V,W) (km s^{-1})	18.4 ± 0.2, −32.6 ± 0.4, 16.5 ± 0.4	This work

Note. *Correction of + 82 μas from Stassun & Torres (2018) applied to the *Gaia* value.

taken in two runs between 2019 May and July, as part of the observing program 1102.C-0923, covering the initial gaps in the orbital phase from the observations in April. We set the exposure time to 1800–2100 s, leading to a mean S/N ratio of ∼40 and a mean uncertainty of ∼1.5 m s^{-1}.

We reduced the spectra using the HARPS online data reduction software (DRS; Bouchy, Pepe & Queloz 2001). The data products include the extracted spectra, both in *echelle* and order-merged spectra, the cross-correlation functions[2] (CCF; Baranne et al. 1996; Pepe et al. 2002) and a measurement of the FWHM of the CCF profile, and the bisector inverse slope (BIS; Queloz et al. 2001).

We extracted the RV measurements using the HARPS–TERRA package (Anglada-Escudé et al. 2012). The algorithm creates a high-S/N template by combining all the observed spectra, based on their S/N ratio, and then it recomputes the RV of a given observation by matching each individual spectrum with the template. One advantage for choosing HARPS–TERRA is that RVs are computed for every echelle order, so it is relatively easy to find the orders with most of the RV information, discarding contaminated or low-S/N orders. In this case, we rejected the 22 bluest orders, and considered only from order 23 to 72 as they produced lowest errors and smallest RMS in the RVs. The software does not compute the BIS nor FWHM of the CCF, which are taken directly from the DRS using a G2 mask. TERRA does compute activity indicators in the form of S-indices directly from each observed spectrum. The S-index is measured from the cores of the Ca II H&K lines ($\lambda_{\rm H}$ = 3933.664 Å, $\lambda_{\rm K}$ = 3968.470 Å) and compared with the flux on adjacent chunks in the continuum, following the prescription from Lovis et al. (2011) and it is calibrated to the Mt. Wilson system ($S_{\rm MW}$), serving as a direct proxy to monitor the chromospheric activity of the star. Uncertainties in BIS are taken as twice the internal RV errors and the FWHM error is 2.35 times the RV uncertainties (see Zechmeister et al. 2013; Santerne et al. 2015). The results are shown in Table 2.

Fig. 2 shows the correlations between RVs and activity indicators, BIS, FWHM CCF, and $S_{\rm MW}$, from left to right, respectively. No significant correlations are seen between the RVs and the activity indicators. However, we note one outlier point in the FWHM and S-index, which was related with an observation acquired under poor weather conditions at the beginning of the observing run in 2019 April.

We computed the generalized Lomb–Scargle periodogram[3] (GLS; Zechmeister & Kürster 2009) of the HARPS Doppler measurements and activity indicators. As shown in Fig. 3, the GLS periodogram of the HARPS RVs shows a significant peak at the orbital period of the transiting planet (2.11 d) with a false-alarm probability FAP < 0.1 per cent. We note that the secondary peak with FAP < 1 per cent (P = 0.7d) is the alias of the orbital period due to the sampling frequency. The periodograms of the HARPS activity indicators show neither a significant peak matching the one found in the RVs, nor any other significant peaks (Fig. 3).

4 STELLAR PARAMETERS

We first estimated the stellar parameters[4] by combining the HARPS spectra into a high-S/N ratio spectrum and fed that into the spectral classification and stellar parameter estimation software package `SPECIES` (Soto & Jenkins 2018). For a more detailed explanation and outputs from this code, the reader is referred to Díaz et al. (2018) and Soto & Jenkins (2018).

We also analysed the combined HARPS spectrum using both Spectroscopy Made Easy (version 5.22; Valenti & Piskunov 1996; Piskunov & Valenti 2017), and the empirical package `SpecMatch-Emp` (Yee, Petigura & von Braun 2017). We followed the same procedures outlined in, e.g. Fridlund et al. (2017), Persson et al. (2018), Persson et al. (2019), and Gandolfi et al. (2019). The two methods provide consistent results within 1σ and 2σ, which are also in agreement with those obtained with `SPECIES`. In particular, the age of the star was determined by isochrone fitting according to the method described in `SPECIES`. We note that, while there is no reason to prefer one set of spectroscopic parameter estimates over the others, we adopted the results derived with `SPECIES` for the subsequent analyses presented in this work.

[2]Obtained using a G2 numerical mask.

[3]`astropy.timeseries.LombScargle()`, https://docs.astropy.org/en/stable/timeseries/lombscargle.html.

[4]Including $v\ sin(i)$ and $v_{\rm mac}$

Downloaded from https://academic.oup.com/mnras/article/493/1/973/5717324 by guest on 13 May 2022

Table 2. HARPS radial velocities and spectral activity indices for TOI-132.

BJD (−2450000)	RV (m s^{-1})	σRV (m s^{-1})	S_{MW} (dex)	σS_{MW} (dex)	FWHM (km s^{-1})	σFWHM (m s^{-1})	BIS (m s^{-1})	σBIS (m s^{-1})
8576.90725	− 4.737	2.967	0.056	0.003	6.885	16.180	2.967	5.933
8578.89655	0.000	2.398	0.128	0.004	6.911	16.240	2.398	4.797
8579.90764	5.631	1.765	0.140	0.003	6.908	16.234	1.765	3.531
8580.90988	− 10.056	1.972	0.121	0.003	6.914	16.248	1.972	3.943
8581.91433	8.808	1.338	0.133	0.002	6.911	16.241	1.338	2.675
8582.91045	− 9.005	1.402	0.135	0.002	6.911	16.241	1.402	2.803
8583.90870	11.771	1.656	0.138	0.003	6.916	16.252	1.656	3.312
8635.81477	− 5.174	2.488	0.151	0.004	6.909	16.235	2.488	4.977
8636.82174	9.069	1.800	0.143	0.003	6.898	16.211	1.800	3.599
8637.91868	2.175	1.649	0.134	0.003	6.914	16.247	1.649	3.297
8642.93057	8.481	1.571	0.145	0.003	6.928	16.281	1.571	3.142
8643.91730	− 10.522	1.129	0.134	0.002	6.911	16.242	1.129	2.257
8644.84072	10.526	1.331	0.139	0.002	6.917	16.256	1.331	2.662
8660.81222	− 13.834	1.945	0.152	0.003	6.905	16.228	1.945	3.891
8664.89377	− 14.864	1.652	0.173	0.004	6.929	16.283	1.652	3.305
8666.80357	− 5.826	1.542	0.165	0.003	6.923	16.270	1.542	3.084
8667.76863	6.145	1.530	0.165	0.003	6.910	16.238	1.530	3.061
8668.82036	− 3.829	1.534	0.156	0.003	6.914	16.249	1.534	3.067
8669.71698	− 0.505	1.294	0.156	0.003	6.916	16.252	1.294	2.588
8669.91776	3.943	1.344	0.137	0.003	6.915	16.250	1.344	2.687

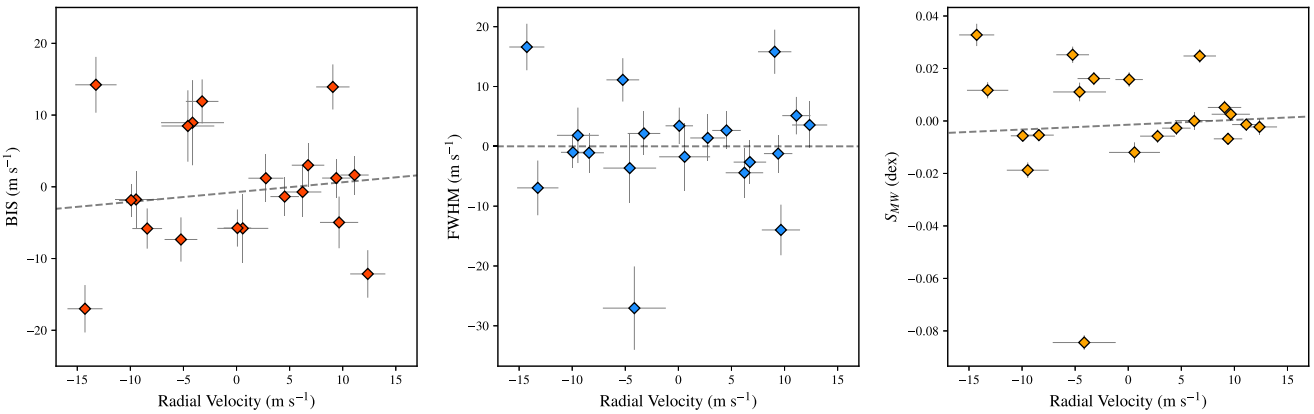


Figure 2. Left to right: correlations between BIS, cross-correlation function FWHM, S-index, and radial velocities after subtraction of their mean, respectively. The first two are obtained from DRS and the latter is derived from the HARPS spectra using the HARPS–TERRA algorithm. On each plot, the dashed line represents a linear fit between the activity index and radial velocity. All three plots show no strong evidence for correlation, although outliers are seen in the FWHM and S_{MW}.

We performed an analysis of the broad-band spectral energy distribution (SED) of the star together with the *Gaia* DR2 parallaxes (adjusted by +0.08 mas to account for the systematic offset reported by Stassun & Torres 2018), in order to determine an empirical measurement of the stellar radius, following the procedures described in Stassun & Torres (2016) and Stassun, Collins & Gaudi (2017), and Stassun et al. (2018a). We retrieved the B_TV_T magnitudes from *Tycho-2*, the *BVgri* magnitudes from APASS, the JHK_S magnitudes from *2MASS*, the W1–W4 magnitudes from *WISE*, and the *G* magnitude from *Gaia*. Together, the available photometry spans the full stellar SED over the wavelength range 0.2–22 μm (see Fig. 4).

We performed a fit using Kurucz stellar atmosphere models, with the effective temperature ($T_{\rm eff}$) and metallicity ([Fe/H]) and surface gravity ($\log g$) adopted from the spectroscopic analysis of SPECIES. The only free parameter is the extinction (A_V), which we restricted to the maximum line-of-sight value from the dust maps of Schlegel, Finkbeiner & Davis (1998). The resulting fit shown in Fig. 4, gives a reduced χ^2 of 2.4 and best-fitting $A_V = 0.03 \pm 0.01$. Integrating the (unreddened) model SED, it gives the bolometric flux at the Earth, $F_{\rm bol} = 7.492 \pm 0.087 \times 10^{-10}$ erg s^{-1} cm^{-2}. Taking the $F_{\rm bol}$ and $T_{\rm eff}$ together with the *Gaia* DR2 parallax, gives the stellar radius, $R_\star = 0.90 \pm 0.02\,{\rm R}_\odot$. Finally, we can use the empirical relations of Torres, Andersen & Giménez (2010) and a 6 per cent error from the empirical relation itself to estimate the stellar mass, $M_\star = 0.97 \pm 0.06\,{\rm M}_\odot$; this, in turn, together with the stellar radius provides an empirical estimate of the mean stellar density $\rho_\star = 1.89 \pm 0.15$ g cm^{-3}. We note the small errorbars on both stellar mass and radius come directly from propagation of uncertainties in $T_{\rm eff}$, $F_{\rm bol}$, and parallax. In this case, the fractional errors are of order

Downloaded from https://academic.oup.com/mnras/article/493/1/973/5717324 by guest on 13 May 2022

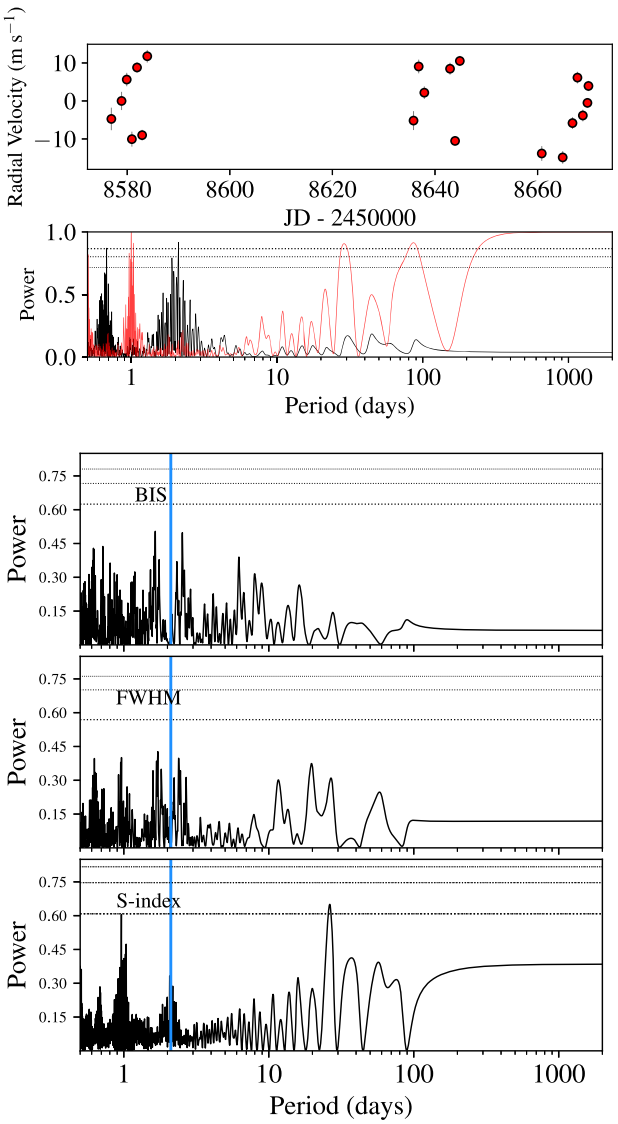


Figure 3. Top panels: Time series showing the radial velocities from the HARPS follow-up observations. Generalized Lomb–Scargle periodogram of the radial velocities. The red power spectrum shows the window function. Bottom panels: Same as top panel but for the activity indices obtained with HARPS: BIS, FWHM, and S-index, respectively. The horizontal lines, from bottom to top on each periodogram, represent the 10, 1, and 0.1 per cent significance levels estimated via 5000 bootstrap samples. The vertical line on each plot marks the position of the 2.11-d planet candidate signal present in the radial velocity.

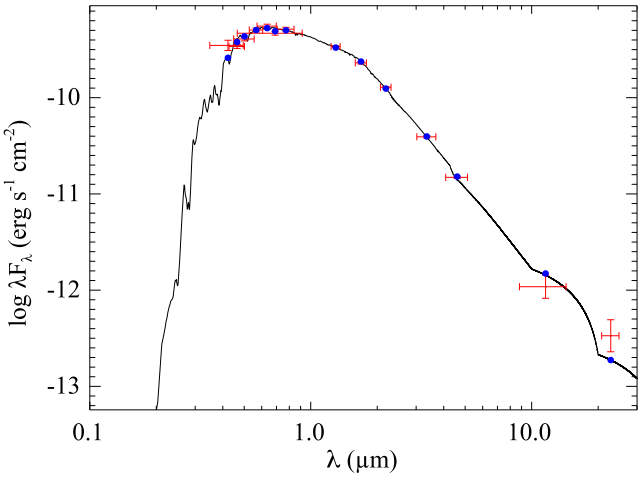


Figure 4. Spectral energy distribution of TOI-132. The blue points are the predicted integrated fluxes and the red symbols are the observed values at the corresponding passbands, where the horizontal bars represent the effective width of the passband and the vertical errors represent the 1σ uncertainties. The best-fitting Kurucz atmospheric model for TOI-132 is shown by the black solid line.

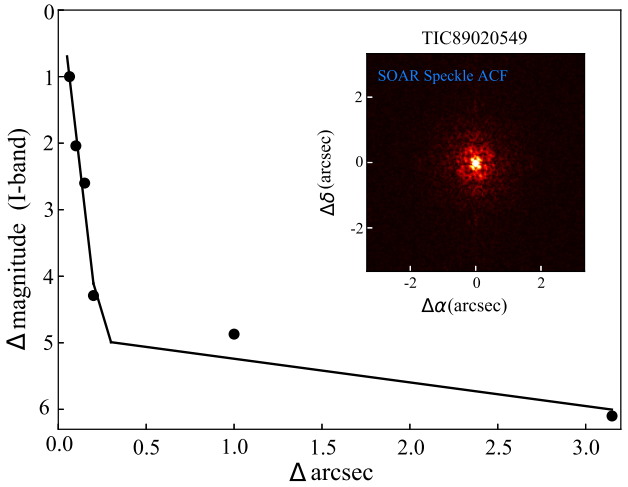


Figure 5. Speckle imaging for TOI-132 obtained with SOAR. Inset on the top right-hand corner shows a preview of the ACF.

$\sim$1 per cent, $\sim$1 per cent, and $\sim$0.5 per cent, respectively. Then, the uncertainty in stellar radius is dominated by the $T_{\rm eff}$ error, in this case that implies an error of $\sim$2 per cent (see Table 1).

5 SPECKLE IMAGING

The relatively large 21-arcsec pixels of *TESS* can result in contamination from companion stars or nearby sources. The additional light from these can dilute the planetary transit, resulting in an underestimated planet radius. We searched for nearby sources with speckle imaging with HRCam on the 4.1-m Southern Astrophysical Research (SOAR) telescope (Tokovinin et al. 2018) on 2018 September 25 UT. From these observations, a potential companion star was detected at low significance. The purported star was located near the first diffraction ring of the primary star, at 0.079 arcsec (and a projected distance of $\sim$12 au), a similar position as optical ghosts that can occasionally appear in the speckle imaging during periods of low wind. This triggered a warning as the flux contamination due to the companion (Δm $\sim$ 2.6 mag) would have not been negligible for the spectroscopic observations given that the diameter of the fibers on HARPS is $\sim$1 arcsec, meaning that the suspected companion was inside the aperture of the fiber. Upon visual inspection of the CCF and the individual spectra, we could not see evidence for such a contamination. The system was observed again on 2019 May 18 UT in excellent conditions, and the possible companion star was not detected. The 5σ detection sensitivity and autocorrelation function of the later observation are shown in Fig. 5.

Downloaded from https://academic.oup.com/mnras/article/493/1/973/5717324 by guest on 13 May 2022

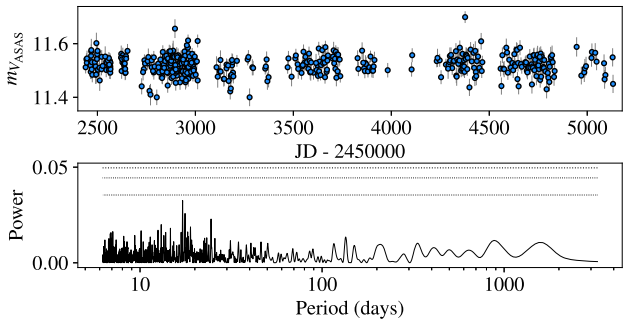


Figure 6. ASAS *V*-band photometry for TOI-132 to search for additional sources of periodicity in the star. The bottom plot shows the Generalized Lomb–Scargle periodogram of the time series. The horizontal lines, from bottom to top, represent the 10, 1, and 0.1 per cent significance levels estimated via 5000 bootstrap samples.

6 ASAS PHOTOMETRY

We analysed photometry from the All-Sky Automated Survey (ASAS; Pojmanski 1997) to search for stellar rotational periods. There are 694 available photometric measurements spanning 8.9 yr, from 2000 November to 2009 December. The selection of the best aperture was made choosing the time series with the lowest median absolute deviation (MAD). We discarded 129 points that were flagged as bad data points, including only 565 measurements with either 'A' or 'B' quality. Fig. 6 shows the photometric time series after removing outliers and bad data and the GLS.[5]

From the power spectrum in the periodogram, the highest power is found to be at 17.138 d. We estimated the 10, 1, and 0.1 per cent significance level by running 5000 bootstrap samplings using the implementation available in the `Python` module `astropy.stats.false_alarm_probability()`.[6] Although the highest peak in the GLS periodogram is noticeable and unique, its significance is below the 10 per cent level, as seen from the bottom panel in the figure. We note that the highest cadence in the photometry is ∼1 d, however, the sampling of the time series is very sparse, making the detection of rotation periods on short time-scales of ∼10–20 d difficult.

7 JOINT ANALYSIS

We modelled the RVs and the photometry using the `juliet`[7] package (Espinoza, Kossakowski & Brahm 2019a). Table 3 shows the priors used in the analysis. We set up the initial priors for the period of the candidate and the time of transit (T_0) using the reported values in the *TESS* DV report document for TOI-132.

Preliminary analysis was done using `Systemic Console v2` (Meschiari et al. 2009). We analysed the RVs only to get an initial rough estimate of both instrumental and orbital parameters of the system such as the velocity semi-amplitude, eccentricity, and minimum mass of the planet. The period and transit time were constrained using the updated values provided by *TESS*. Initial results for a one-planet model with eccentricity fixed at zero, yields an RMS ∼ 2.7 m s^{-1}. Letting eccentricity and argument of periastron as free parameters the best-fitting model RMS goes down to ∼2.5 m s^{-1} and e ∼ 0.17. We then performed further analyses considering two scenarios (circular and eccentric) with `juliet`. This package has been proven to be an excellent tool for analysing both photometry and RVs using a joint model (see e.g. Brahm et al. 2019; Espinoza et al. 2019b; Kossakowski et al. 2019). In short, the code uses `batman` (Kreidberg 2015) to model the transit data and `radvel` (Fulton et al. 2018) to model the RVs, and in order to estimate the Bayesian log-evidence, ln$Z$, for model comparison we used the option of the Dynamic Nested Sampling algorithm that the `dynesty` (Speagle & Barbary 2018; Speagle 2020) package provides. We note that, while `juliet` has the option to include Gaussian Processes to model the light curve, RVs, or both, we did not set this option as there was no evidence of additional variability in the `PDCSAP_FLUX`-corrected light curve (see Fig. 1). We also used the parametrization described in Espinoza (2018) that allows an efficient way to sample the impact parameter, b, and the planet-to-star radius ratio, p, where only values that are physically plausible in the (p, b) plane are sampled via the r_2 and r_2 coefficients (Espinoza 2018). For the limb-darkening coefficients, we use the parametrization of Kipping (2013) for two-parameter laws. Speckle images obtained for TOI-132 rules out the possibility of significant nearby sources of light. Therefore, we fixed the dilution factor to a value of 1 for the photometric data sets. The priors and boundaries for the parameters used in the joint analysis are listed in Table 3.

We set up two different runs, first by fixing eccentricity to zero, and another treating it (along with ω) as free parameter. Comparing the evidences from the circular (ln$Z$ = 89705.63) and eccentric model (ln$Z$ = 89706.85), we obtain $\Delta\ln Z = 1.22$ that suggests weak evidence the latter is preferred over the circular model according to the model selections criteria and thresholds described in Espinoza et al. (2019a). The joint model results are shown in Fig. 7 and the best fit, or most probable parameters given the data are listed in Table 4. The quoted values are the median value from the posterior distribution.

As a sanity check, we also performed an independent joint analysis using the `Python/FORTRAN` software suite `pyaneti` (Barragán, Gandolfi & Antoniciello 2019a). Results are consistent with those obtained with `juliet` well within the nominal error bars.

Using the luminosity of the host star, we could retrieve the incident flux on TOI-132 b using the semimajor axis from our joint model. We estimated that the insolation of TOI-132 b is $S_p = 860\, S_\oplus$.

In order to estimate the average equilibrium temperature of the planet, considering the physical properties of TOI-132 b we assumed a Bond albedo of $A_B = 0.31$, which corresponds to the value accepted for Neptune. Then,

$$T_{eq} = T_* \sqrt{\frac{R_*}{2a}} (1 - A_B)^{\frac{1}{4}} \quad (1)$$

yields an equilibrium temperature of $T_{eq} = 1395^{+52}_{-72}\, K$ for the planet.

8 TTV ANALYSIS

In order to search for possible TTVs in TOI-132 b, we computed the individual transit time of each light curve using the `EXOFASTv2` code (Eastman, Gaudi & Agol 2013; Eastman 2017). `EXOFASTv2` uses the Differential Evolution Markov chain Monte Carlo method to derive the values and their uncertainties for the stellar, orbital, and physical parameters of the system.

[5] MAD = median($|X_i - \tilde{X}|$)/0.6745
[6] https://docs.astropy.org/en/stable/timeseries/lombscargle.html
[7] https://github.com/nespinoza/juliet

Downloaded from https://academic.oup.com/mnras/article/493/1/973/5717324 by guest on 13 May 2022

Table 3. Below are the priors used for TOI-132 for the *final* joint analysis fit using `juliet`. As a reminder, $p = R_p/R_*$ and $b = (a/R_*)\cos(i_p)$, where R_p is the planetary radius, R_* the stellar radius, a the semimajor axis of the orbit, and i_p the inclination of the planetary orbit with respect to the plane of the sky. e and ω are the eccentricity and argument of periastron of the orbits. The prior labels of $\mathcal{N}, \mathcal{U}$, and $\mathcal{J}$ represent normal, uniform, and Jeffreys distributions. See text for explanations about other parameters.

Parameter name	Prior	Units	Description
Parameters for planet b			
P_b	$\mathcal{N}(2.10937, 0.001)$	d	Period.
$T_{0,b} - 2458000$	$\mathcal{N}(337.451, 10)$	d	Time of transit centre.
$r_{1,b}$	$\mathcal{U}(0, 1)$	–	Parametrization for p and b^a.
$r_{2,b}$	$\mathcal{U}(0, 1)$	–	Parametrization for p and b^a.
a_b	$\mathcal{U}(4.5, 7.0)$	–	Scaled semimajor axis.
K_b	$\mathcal{U}(1, 100)$	m s^{-1}	Radial-velocity semi-amplitude.
e_b	$\mathcal{U}(0, 1)$	–	Eccentricity.
ω_b	$\mathcal{U}(0, 359)$	deg	Argument of periastron.
Parameters for *TESS*			
$D_{\rm TESS}$	1.0 (Fixed)	–	Dilution factor for *TESS*.
$M_{\rm TESS}$	$\mathcal{N}(0, 1)$	ppm	Relative flux offset for *TESS*.
$\sigma_{w,\rm TESS}$	$\mathcal{J}(0.1, 100)$	ppm	Extra jitter term for *TESS* light curve.
$q_{1,\rm TESS}$	$\mathcal{U}(0, 1)$	–	Quadratic limb-darkening parametrization.
$q_{2,\rm TESS}$	$\mathcal{U}(0, 1)$	–	Quadratic limb-darkening parametrization.
Parameters for LCOGT			
$D_{\rm LCOGT}$	1.0 (Fixed)	–	Dilution factor for LCOGT.
$M_{\rm LCOGT}$	$\mathcal{N}(0, 1)$	ppm	Relative flux offset for LCOGT.
$\sigma_{w,\rm LCOGT}$	$\mathcal{J}(0.1, 100)$	ppm	Extra jitter term for LCOGT light curve.
$q_{1,\rm LCOGT}$	$\mathcal{U}(0, 1)$	–	Quadratic limb-darkening parametrization.
$q_{2,\rm LCOGT}$	$\mathcal{U}(0, 1)$	–	Quadratic limb-darkening parametrization.
Parameters for HARPS			
$\mu_{\rm HARPS}$	$\mathcal{N}(-0.6, 1.)$	m s^{-1}	Radial velocity zero-point (offset).
$\sigma_{w,\rm HARPS}$	$\mathcal{J}(0.1, 10)$	m s^{-1}	Extra jitter term for HARPS radial velocities.

Note. [a]We used the transformations outlined in Espinoza (2018) and also set $p_l = 0.03$ and $p_u = 0.05$ in the `juliet` call.

So, to obtain the transit time of each light curve, we fixed the stellar and orbital parameters to the values obtained from the global fit performed by `juliet`, except for the transit time and their baseline flux. If a planet follows strictly a Keplerian orbit, the transit time of a given epoch $T_c(E)$ is a linear function of the orbital period P:

$$T_c(E) = T_0 + P \times E, \tag{2}$$

where T_0 is a reference transit time and E is the number of epochs since T_0. The best-fitting values for equation (2) from `juliet` are shown in Table 4 along with the planetary parameters fixed to compute the individual transit time.

Considering the theoretical and the observed transit times of the light curves, we obtained the TTV values for TOI-132 b presented in Fig. 8. Even though the larger variation is about 22 min, we found no evidence of a clear periodic variation in the transit time. This outlier is probably induced by a gap in the light curve of epoch 5. The RMS variation from the linear ephemeris is $\sigma = 8.03$ min, however, the reduced chi-squared for this model is $\chi^2_{\rm red} = 1.37$. This is an indicator that the transit times, considering their errors, fit well with the proposed linear ephemeris.

The lack of an additional RV signal, as well as no evidence of a TTV signal for our given time span of our transit data, suggests that there is no other close-in companion of TOI-132 b. These results also rule out additional planets in low-order resonant configurations with TOI-132 b. Nevertheless, further ground-based follow-up will be required to unveil the possible existence of companions in TOI-132.

9 DISCUSSION AND CONCLUSIONS

By combining *TESS* space-based photometry with HARPS high-precision RV measurements, along with additional high-sensitivity ground-based photometric observations, we were able to confirm a short period, hot Neptune-like planet orbiting the nearby metal-rich G8V star TOI-132. The planet was found to have an orbital period of only 2.1 d, a radius of $3.42^{+0.13}_{-0.14}$ $R_\oplus$, and mass of $22.40^{+1.90}_{-1.92}$ $M_\oplus$, implying a density and equilibrium temperature of $3.08^{+0.44}_{-0.46}$ g cm^{-3} and 1395^{+52}_{-72} K, respectively.

In Fig. 9, we can see that TOI-132 b is located in an under-populated region of the mass–radius diagram. Of the relatively small number of known Neptune-like planets with well-constrained properties, TOI-132 b stands out as bridging the gap between 100 per cent water worlds and more typical Neptunes that have atmospheric mass fractions of ∼10 per cent. The planet likely more closely resembles NGTS-4 b (West et al. 2019), which is shown in the figure despite the relatively high uncertainties measured for the planetary parametsers, or TOI-824 b (Burt et al., private communication). These three planets appear to have similar masses and radii, giving rise to similar densities and bulk

Downloaded from https://academic.oup.com/mnras/article/493/1/973/5717324 by guest on 13 May 2022

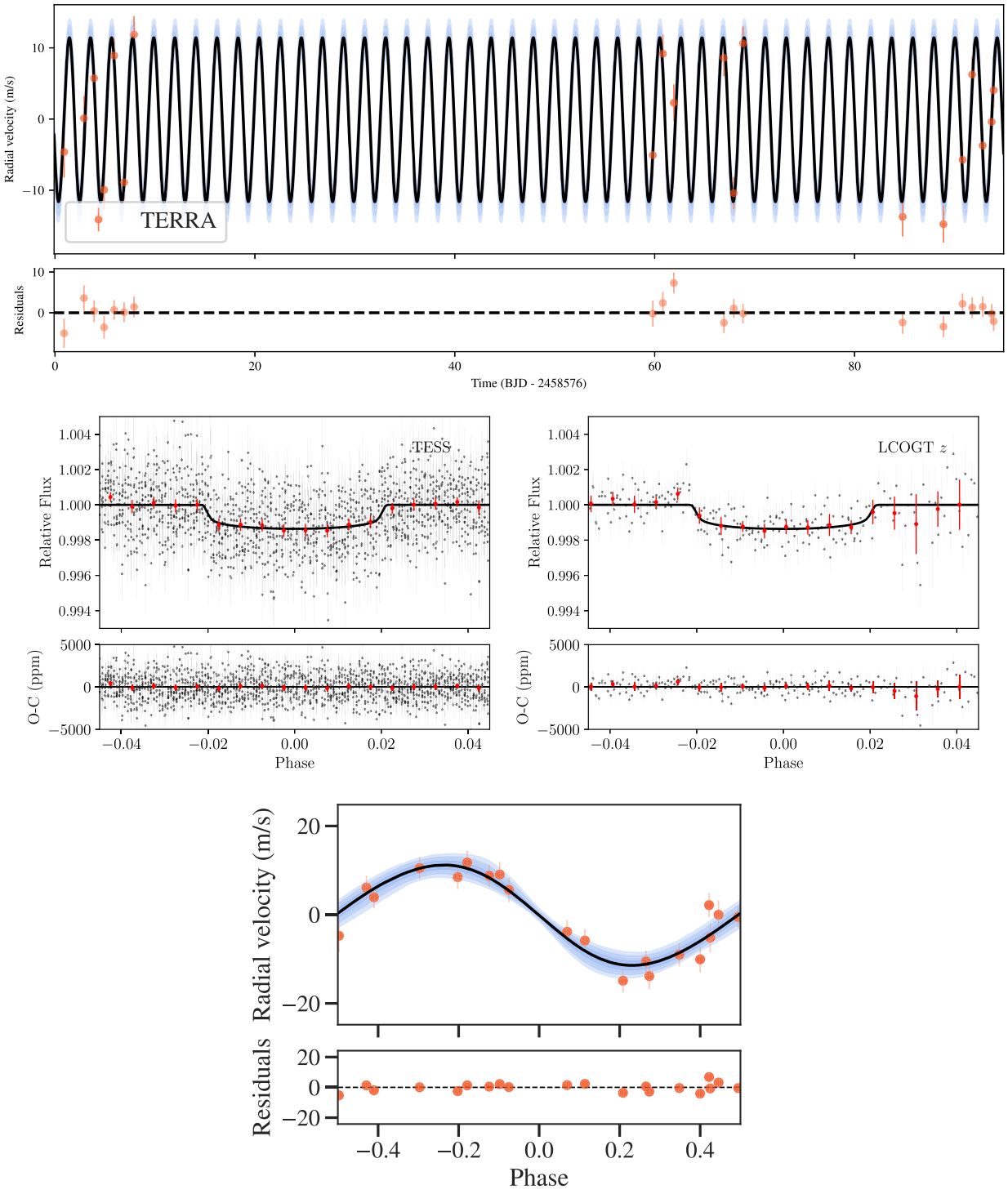


Figure 7. Results from the joint fit for the one-planet model. *Top panel:* HARPS–TERRA radial velocities and best-fitting Keplerian model (the solid curve) the bands around it show 68 per cent, 95 per cent, and 99 per cent posterior credibility bands. *Mid panels: TESS* photometry (left) and LCOGT z-short photometry (right) phase-folded to the 2.109 d period of TOI-132 b along with best-fitting transit model from the joint fit. The red points show the binned photometry in phase bins of 0.005. *Bottom panel:* phase-folded RVs from HARPS. The black line shows the model. Credibility bands are shown in the same way as in top panel. Best-fitting parameters are the most probable parameters given the data and the quoted values are the median value from the posterior distribution. The error bars of both photometry and RV data include their corresponding jitter.

Downloaded from https://academic.oup.com/mnras/article/493/1/973/5717324 by guest on 13 May 2022

Table 4. Planetary properties for TOI-132 b.

Property	Value
Fitted parameters	
P (d)	$2.1097019^{+0.000012}_{-0.000011}$
T_0 (BJD - 2450000)	$8333.23095^{+0.00094}_{-0.00096}$
a/R_*	$6.362^{+0.413}_{-0.627}$
b	$0.533^{+0.124}_{-0.137}$
K ($m\,s^{-1}$)	$11.38^{+0.84}_{-0.85}$
i_p (deg)	$85.03^{+1.30}_{-1.84}$
e	$0.059^{+0.050}_{-0.037}$
ω (deg)	$125.88^{+57.23}_{-38.05}$
Derived parameters	
M_p ($M_\oplus$)	$22.40^{+1.90}_{-1.92}$
R_p ($R_\oplus$)	$3.42^{+0.13}_{-0.14}$
a (AU)	$0.026^{+0.002}_{-0.003}$
ρ_p (g cm^{-3})	$3.08^{+0.44}_{-0.46}$
T^a_{eq} (K)	1395^{+52}_{-72}
Instrumental parameters	
M_{TESS} (ppm)	$-0.000069^{+0.000011}_{-0.000012}$
$\sigma_{w,TESS}$ (ppm)	$10.58^{+27.14}_{-8.14}$
$q_{1,TESS}$	$0.361^{+0.344}_{-0.242}$
$q_{2,TESS}$	$0.331^{+0.342}_{-0.223}$
M_{LCOGT} (ppm)	$-0.000057^{+0.000060}_{-0.000057}$
$\sigma_{w,LCOGT}$ (ppm)	$462.35^{+72.73}_{-73.70}$
$q_{1,LCOGT}$	$0.426^{+0.309}_{-0.262}$
$q_{2,LCOGT}$	$0.284^{0.296}_{-0.186}$
μ_{HARPS} (m s^{-1})	$-0.18^{+0.51}_{-0.55}$
$\sigma_{w,HARPS}$ (m s^{-1})	$2.00^{+0.72}_{-0.64}$

Note. [a]Estimated using a Bond albedo of 0.31 (see text).

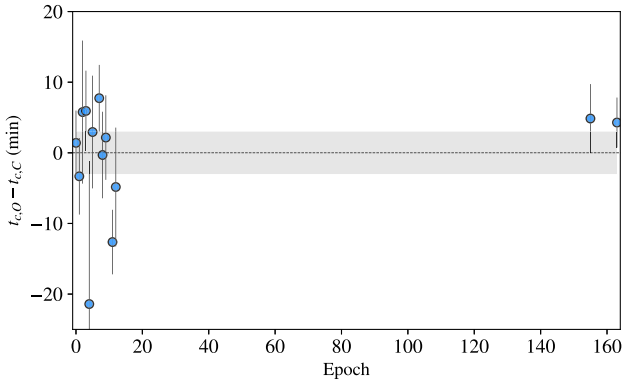


Figure 8. Observed minus computed mid-transit times of TOI-132 b. The residuals (TTV) of the transit times are shown considering the proposed linear ephemeris. The dashed line corresponds to zero variation and the grey area is the propagation of 1σ uncertainties, considering the optimal transit time from `EXOFASTv2`, and the period from `juliet`. The epoch 0 is the first transit observed by *TESS* and it is also the corresponding epoch of the optimal transit time. The TTV values shown in this plot fit accordingly with the proposed linear ephemeris ($\chi^2_{red} = 1.37$).

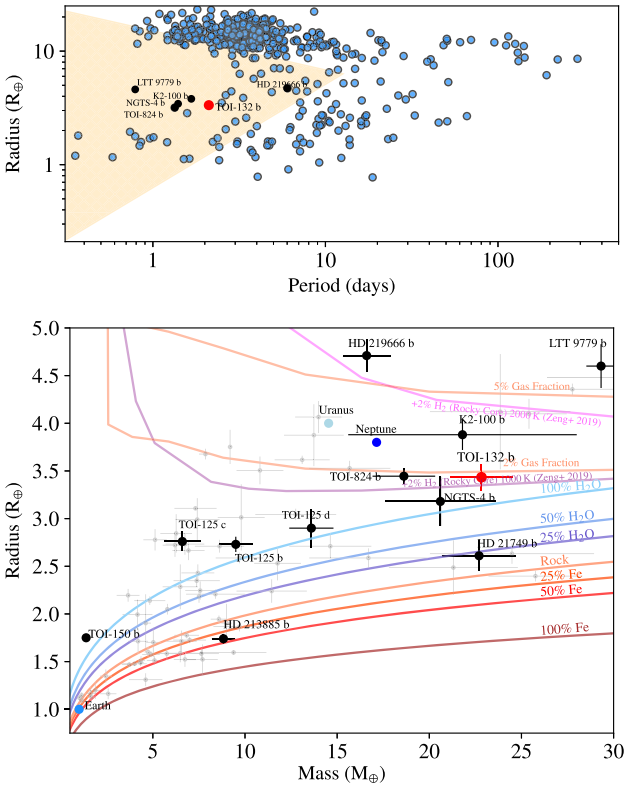


Figure 9. *Top*: Period–radius diagram for planets whose radius has been measured with a precision better than 5 per cent. We have included recent *TESS* discoveries (Burt et al., private communication; Nielsen et al. 2020). The shaded area indicates the Neptune desert where the edges are defined by Mazeh et al. (2016). TOI-132 b is highlighted with a red circle, near the edge of the desert. *Bottom*: Mass–radius diagram for planets whose mass and radius have been measured with a precision better than 25 per cent (the grey circles) in the range $R_p < 5R_\oplus$ and $M_p < 30M_\oplus$, retrieved from the transiting planets catalog `TEPCat` (available at https://www.astro.keele.ac.uk/jkt/tepcat/, Southworth 2011). The black points show recent discoveries from *TESS*. TOI-132 b is shown with a red circle. The solid, coloured lines show models for different compositions from Zeng, Sasselov & Jacobsen (2016) ranging from 100 per cent iron core planet to 100 per cent H_2O planet. Also, two-layer models from Zeng et al. (2019) are shown for 2 per cent H_2 envelopes at different temperatures (magenta, purple). Extended models (Lopez & Fortney 2014) are shown for 95 per cent and 98 per cent core mass fraction, 6.2 Gyr (orange).

compositions, which might indicate they share similar formation histories.

Moreover, it is interesting to mention the planet K2-100 b from the *K2* mission (Mann et al. 2017). Recently characterized by Barragán et al. (2019b), the planet consists of a young, inflated Neptune on a short period around a G-type star. TOI-132 b falls within the evolutionary range of K2-100 b after 5 Gyr. This may indicate in the past TOI-132 b could have shared similar characteristics to that of K2-100 b, and at some point given the strong stellar irradiation on TOI-132 b could have caused atmospheric loss we see in the present. Hence, TOI-132 b is an interesting target for atmospheric transit spectroscopy, to check for evidence of ongoing atmospheric loss through a wind.

While TOI-132 b is not as extreme in some respects as the recently discovered, first ultrahot Neptune LTT 9779 b (Jenkins et al. 2020), it is placed right at the edge of the Neptune desert.

Downloaded from https://academic.oup.com/mnras/article/493/1/973/5717324 by guest on 13 May 2022

The survival of the planet's atmosphere can likely be understood based on its large core mass, and also the incompatibility with being composed of either 100 per cent rock or water. This would imply that, at the present time, TOI-132 b could maintain some significant gaseous atmosphere. We employed a 1D thermal evolution model (Lopez & Fortney 2014), and for an Earth-like rocky core we find a best-fitting current day atmospheric mass fraction of $4.3^{+1.2}_{-2.3}$ per cent gas, which can be retained with an initial envelope fraction of ~ 9 per cent at 10 Myr. We note here that rocky core likely consists of a combination of rock and iron even if the relative core mass fraction is not clear. Moreover, these results are model dependent rather than being directly constrained by the data.

With the *Gaia* parameters from Table 1, we calculated the star's Galactic space motion. We used the `IDL` routine `calc_uvw`, based upon Johnson & Soderblom (1987) and the local standard of rest from Coşkunoğlu et al. (2011), we obtained (U,V,W) = (18.4 ± 0.2, -32.6 ± 0.4, 16.5 ± 0.4) km s^{-1}. Per the methodology of Reddy, Lambert & Allende Prieto (2006), this corresponds to a 98 per cent probability that TOI-132 belongs to the Galactic thin disc, which is consistent with the relatively high [Fe/H] we measured for the star.

The relatively high metallicity of the host star can also help to explain the large core mass fraction of the planet. Such metal-rich discs can quickly build up high-mass cores that can accumulate large fractions of gas before the disc is dispersed on time-scales of ∼5–10 Myr (Baraffe, Chabrier & Barman 2010; Mulders 2018). Indeed, we may expect more cores to have been formed in this process, possibly influencing the migration history of TOI-132 b, and therefore future precision RV measurements should be sought to search for the presence of a more rich planetary system.

In this paper, we have presented the *TESS* discovery of a Neptune-sized planet transiting the G-type star TOI-132 on the edge of the Neptune desert. Confirmation of this candidate comes from high-precision HARPS spectroscopic observations that fully constrain the orbital and physical parameters of TOI-132 b. Additional ground-based photometry and speckle images provide evidence of the planetary nature of TOI-132 b.

Structure models suggest that the planet can have a rocky core, retaining an atmospheric mass fraction of $4.3^{+1.2}_{-2.3}$ per cent. TOI-132 b stands as a *TESS* Level 1 Science Requirement candidate, which aims to precisely measure the masses for 50 transiting planets smaller than $4R_\oplus$. Therefore, future follow-up observations will allow the search for additional planets in the TOI-132 system, and also will help to constrain low-mass planet formation and evolution models, key to understanding the Neptune desert.

ACKNOWLEDGEMENTS

MRD acknowledges support of CONICYT-PFCHA/Doctorado Nacional-21140646 and Proyecto Basal AFB-170002. JSJ is supported by FONDECYT grant 1161218 and partial support from CATA-Basal (PB06, CONICYT). ZMB acknowledges funds from CONICYT-FONDECYT/Chile Postdoctorado 3180405. JIV acknowledges support of CONICYT- PFCHA/Doctorado Nacional-21191829, Chile. ME acknowledges the support of the DFG priority program SPP 1992 'Exploring the Diversity of Extrasolar Planets' (HA 3279/12-1). KWFL, SzCs acknowledge support by DFG grant RA 714/14-1 within the DFG Schwerpunkt SPP 1992, 'Exploring the Diversity of Extrasolar Planets'. LGC acknowledges support from the MINECO FPI-SO doctoral research project SEV-2015-0548-17-2 and predoctoral contract BES-2017-082610. SM acknowledges support from the Spanish Ministry under the Ramon y Cajal fellowship number RYC-2015-17697. NN acknowledges support by JSPS KAKENHI grant JP18H01265 and JP18H05439, and JST PRESTO grant JPMJPR1775. AS acknowledges financial support from the French Programme National de Planétologie (PNP, INSU). Funding for the *TESS* mission is provided by NASA's Science Mission directorate. We acknowledge the use of *TESS* Alert data, from pipelines at the *TESS* Science Office and at the *TESS* SPOC. Resources supporting this work were provided by the NASA High-End Computing Program through the NASA Advanced Supercomputing Division at Ames Research Center for the production of the SPOC data products. This research has used the Exoplanet Follow-up Observation Program website, which is operated by the California Institute of Technology, under contract with the National Aeronautics and Space Administration under the Exoplanet Exploration Program. This work uses observations from the LCOGT network.

REFERENCES

Anglada-Escudé G. et al., 2012, ApJ, 751, L16
Baraffe I., Chabrier G., Barman T., 2010, Rep. Prog. Phys., 73, 016901
Baranne A. et al., 1996, A&AS, 119, 373
Barragán O., Gandolfi D., Antoniciello G., 2019a, MNRAS, 482, 1017
Barragán O. et al., 2019b, MNRAS, 490, 698
Batalha N. M. et al., 2013, ApJS, 204, 24
Beaugé C., Nesvorný D., 2013, ApJ, 763, 12
Benítez-Llambay P., Masset F., Beaugé C., 2011, A&A, 528, A2
Borucki W. J., 2010, APS April Meeting Abstracts, #V1.002
Bouchy F., Pepe F., Queloz D., 2001, A&A, 374, 733
Brahm R. et al., 2019, AJ, 158, 45
Brown T. M. et al., 2013, PASP, 125, 1031
Ceillier T. et al., 2017, A&A, 605, A111
Chen H., Rogers L. A., 2016, ApJ, 831, 180
Collins K. A., Kielkopf J. F., Stassun K. G., Hessman F. V., 2017, AJ, 153, 77
Coşkunoğlu B. et al., 2011, MNRAS, 412, 1237
Díaz M. R. et al., 2018, AJ, 155, 126
Eastman J., 2017, Astrophysics Source Code Library, record ascl:1710.003
Eastman J., Gaudi B. S., Agol E., 2013, PASP, 125, 83
Espinoza N., 2018, Research Notes of the American Astronomical Society, Vol. 2, Efficient Joint Sampling of Impact Parameters and Transit Depths in Transiting Exoplanet Light Curves . p. 209
Espinoza N. et al., 2016, AJ, 152, 108
Espinoza N., Kossakowski D., Brahm R., 2019a, MNRAS, 490, 2262
Espinoza N. et al., 2019b, MNRAS, 491, 2982
Esposito M. et al., 2019, A&A, 623, A165
Fridlund M. et al., 2017, A&A, 604, A16
Fulton B. J. et al., 2017, AJ, 154, 109
Fulton B. J., Petigura E. A., Blunt S., Sinukoff E., 2018, PASP, 130, 044504
Gandolfi D. et al., 2019, ApJ, 876, L24
García R. A. et al., 2014, A&A, 572, A34
Helled R., Lozovsky M., Zucker S., 2016, MNRAS, 455, L96
Huang C. X. et al., 2018, ApJ, 868, L39
Jenkins J. M., 2002, ApJ, 575, 493
Jenkins J. M., 2017, Technical report, Kepler Data Processing Handbook: Overview of the Science Operations Center. NASA Ames Research Center, Moffett Field CA
Jenkins J. M. et al., 2010, in Radziwill N. M., Bridger A., eds, Proc. SPIE Conf. Ser. Vol. 7740, Software and Cyberinfrastructure for Astronomy. SPIE, Bellingham, p. 77400D
Jenkins J. M. et al., 2016, in Chiozzi G., Guzman J. C., eds, Proc. SPIE Conf. Ser. Vol. 9913, Software and Cyberinfrastructure for Astronomy IV. SPIE, Bellingham, p. 99133E
Jenkins J. S. et al., 2020, Nature Astronomy, in review

Downloaded from https://academic.oup.com/mnras/article/493/1/973/5717324 by guest on 13 May 2022

Jensen E., 2013, Astrophysics Source Code Library, record ascl:1306.007
Jin S., Mordasini C., Parmentier V., van Boekel R., Henning T., Ji J., 2014, ApJ, 795, 65
Johnson D. R. H., Soderblom D. R., 1987, AJ, 93, 864
Kipping D. M., 2013, MNRAS, 435, 2152
Kossakowski D. et al., 2019, MNRAS, 490, 1094
Kreidberg L., 2015, PASP, 127, 1161
Li J., Tenenbaum P., Twicken J. D., Burke C. J., Jenkins J. M., Quintana E. V., Rowe J. F., Seader S. E., 2019, PASP, 131, 024506
Lopez E. D., Fortney J. J., 2013, ApJ, 776, 2
Lopez E. D., Fortney J. J., 2014, ApJ, 792, 1
Lovis C. et al., 2011, preprint (arXiv:1107.5325)
Lundkvist M. S. et al., 2016, Nat. Commun., 7, 11201
Luque R. et al., 2019, A&A, 623, A114
Mann A. W. et al., 2017, AJ, 153, 64
Marcy G. W. et al., 2014, ApJS, 210, 20
Mathur S. et al., 2010, A&A, 511, A46
Mayo A. W. et al., 2019, AJ, 158, 165
Mazeh T., Holczer T., Faigler S., 2016, A&A, 589, A75
McCully C. et al., 2018, LCOGT/banzai: Initial Release. Available at: Zenodo.org/record/1257560
Meschiari S., Wolf A. S., Rivera E., Laughlin G., Vogt S., Butler P., 2009, PASP, 121, 1016
Mulders G. D., 2018, Planet Populations as a Function of Stellar Properties. Springer International Publishing AG, Springer Nature, p. 153
Nielsen L. D. et al., 2020, MNRAS, in press
Owen J. E., Lai D., 2018, MNRAS, 479, 5012
Owen J. E., Wu Y., 2013, ApJ, 775, 105
Palle E. et al., 2019, A&A, 623, A41
Pepe F. et al., 2002, The Messenger, 110, 9
Persson C. M. et al., 2018, A&A, 618, A33
Persson C. M. et al., 2019, A&A, 628, A64
Petigura E. A., Howard A. W., Marcy G. W., 2013, Proc. Natl. Acad. Sci., 110, 19273
Piskunov N., Valenti J. A., 2017, A&A, 597, A16
Pojmanski G., 1997, Acta Astron., 47, 467
Queloz D. et al., 2001, A&A, 379, 279
Reddy B. E., Lambert D. L., Allende Prieto C., 2006, MNRAS, 367, 1329
Ricker G. R. et al., 2015, J. Astron. Telesc. Instrum. Syst., 1, 014003
Santerne A. et al., 2015, MNRAS, 451, 2337
Santos A. R. G., García R. A., Mathur S., Bugnet L., van Saders J. L., Metcalfe T. S., Simonian G. V. A., Pinsonneault M. H., 2019, ApJS, 244, 21
Schlegel D. J., Finkbeiner D. P., Davis M., 1998, ApJ, 500, 525
Smith J. C. et al., 2012, PASP, 124, 1000
Soto M. G., Jenkins J. S., 2018, A&A, 615, A76
Southworth J., 2011, MNRAS, 417, 2166
Speagle J. S., 2020, MNRAS, preprint (arXiv:1904.02180)
Speagle J. S., Barbary K., 2018, Astrophysics Source Code Library, record ascl:1809.013
Stassun K. G., Torres G., 2016, AJ, 152, 180
Stassun K. G., Torres G., 2018, ApJ, 862, 61
Stassun K. G., Collins K. A., Gaudi B. S., 2017, AJ, 153, 136
Stassun K. G., Corsaro E., Pepper J. A., Gaudi B. S., 2018a, AJ, 155, 22
Stassun K. G. et al., 2018b, AJ, 156, 102
Stumpe M. C., Smith J. C., Catanzarite J. H., Van Cleve J. E., Jenkins J. M., Twicken J. D., Girouard F. R., 2014, PASP, 126, 100
Szabó G. M., Kiss L. L., 2011, ApJ, 727, L44
Tokovinin A., Mason B. D., Hartkopf W. I., Mendez R. A., Horch E. P., 2018, AJ, 155, 235
Torres G., Andersen J., Giménez A., 2010, A&AR, 18, 67
Twicken J. D. et al., 2018, American Astronomical Society Meeting Abstracts #232, p. 120.04
Valenti J. A., Piskunov N., 1996, A&AS, 118, 595
Van Eylen V., Agentoft C., Lundkvist M. S., Kjeldsen H., Owen J. E., Fulton B. J., Petigura E., Snellen I., 2018, MNRAS, 479, 4786
West R. G. et al., 2019, MNRAS, 486, 5094
Wheatley P. J. et al., 2018, MNRAS, 475, 4476
Yee S. W., Petigura E. A., von Braun K., 2017, ApJ, 836, 77
Zechmeister M., Kürster M., 2009, A&A, 496, 577
Zechmeister M. et al., 2013, A&A, 552, A78
Zeng L., Sasselov D. D., Jacobsen S. B., 2016, ApJ, 819, 127
Zeng L. et al., 2019, Proc. Natl. Acad. Sci., 116, 9723

[1]*Departamento de Astronomía, Universidad de Chile, Camino El Observatorio 1515, Las Condes, Santiago, Chile*
[2]*Dipartimento di Fisica, Università degli Studi di Torino, via Pietro Giuria 1, I-10125 Torino, Italy*
[3]*NASA Goddard Space Flight Center, Greenbelt, 20771 MD, USA*
[4]*School of Physics and Astronomy, Queen Mary University of London, G.O. Jones Building, 327 Mile End Road, London E1 4NS, UK*
[5]*Department of Physics & Astronomy, Vanderbilt University, 6301 Stevenson Center Ln., Nashville, TN 37235, USA*
[6]*Department of Physics, Fisk University, 1000 17th Ave. N., Nashville, TN 37208, USA*
[7]*Center for Astrophysics | Harvard & Smithsonian, 60 Garden Street, Cambridge, MA 02138, USA*
[8]*Dunlap Institute for Astronomy and Astrophysics, University of Toronto, ON M5S 3H4, Canada*
[9]*Department of Space, Earth and Environment, Chalmers University of Technology, Onsala Space Observatory, SE- 439 92 Onsala, Sweden*
[10]*Leiden Observatory, University of Leiden, PO Box 9513, NL-2300 RA Leiden, The Netherlands*
[11]*Department of Physics & Astronomy, Swarthmore College, Swarthmore, PA 19081, USA*
[12]*Instituto de Astrofísica de Canarias, Vía Láctea s/n, E-38205 La Laguna, Tenerife, Spain*
[13]*Departamento de Astrofísica, Universidad de La Laguna, San Cristobal de La Laguna, E-38200 S/C de Tenerife, Spain*
[14]*CNRS, CNES, LAM, Aix Marseille University, 13013 Marseille, France*
[15]*Department of Physics, University of Warwick, Gibbet Hill Road, Coventry CV4 7AL, UK*
[16]*Centre for Exoplanets and Habitability, University of Warwick, Gibbet Hill Road, Coventry CV4 7AL, UK*
[17]*Thüringer Landessternwarte Tautenburg, Sternwarte 5, D-07778 Tautenburg, Germany*
[18]*Las Cumbres Observatory, 6740 Cortona Dr., Ste. 102, Goleta, CA 93117, USA*
[19]*Center for Astronomy and Astrophysics, Technical University Berlin, Hardenbergstr 36, D-10623 Berlin, Germany*
[20]*Department of Astronomy, University of Tokyo, 7-3-1 Hongo, Bunkyo-ku, Tokyo 113-0033, Japan*
[21]*Mullard Space Science Laboratory, University College London, Holmbury St Mary, Dorking, Surrey RH5 6NT, UK*
[22]*Department of Astrophysical Sciences, Princeton University, 4 Ivy Lane, Princeton, NJ 08540, USA*
[23]*Astrobiology Center, 2-21-1 Osawa, Mitaka, Tokyo 181-8588, Japan*
[24]*JST, PRESTO, 2-21-1 Osawa, Mitaka, Tokyo 181-8588, Japan*
[25]*National Astronomical Observatory of Japan, 2-21-1 Osawa, Mitaka, Tokyo 181-8588, Japan*
[26]*Cerro Tololo Inter-American Observatory, Casilla 603, La Serena, Chile*
[27]*George Mason University, 4400 University Drive, Fairfax, VA, 22030, USA*
[28]*German Aerospace Center, Institute of Planetary Research, Rutherfordstrasse 2, D-12489 Berlin, Germany*
[29]*MIT Kavli Institute for Astrophysics and Space Research, Massachusetts Institute of Technology, 77 Massachusetts Avenue, 37-241, Cambridge, MA 02139, USA*
[30]*Physics Department and Tsinghua Centre for Astrophysics, Tsinghua University, Beijing 100084, China*
[31]*IRFU, CEA, Université Paris-Saclay, F-91191 Gif-sur-Yvette, France*
[32]*AIM, CEA, CNRS, Université Paris-Saclay, Université Paris Diderot, Sorbonne Paris Cité, F-91191 Gif-sur-Yvette, France*

Downloaded from https://academic.oup.com/mnras/article/493/1/973/5717324 by guest on 13 May 2022

[33]*Department of Earth, Atmospheric and Planetary Sciences, Massachusetts Institute of Technology, Cambridge, MA 02139, USA*
[34]*NASA Ames Research Center, Moffet Field, CA 94035, USA*
[35]*Department of Physics and Astronomy, University of North Carolina at Chapel Hill, Chapel Hill, NC 27599-3255, USA*
[36]*SETI Institute, 189 Bernardo Ave, Suite 200, Mountain View, CA 94043, USA*
[37]*Department of Aeronautics and Astronautics, MIT, 77 Massachusetts Avenue, Cambridge, MA 02139, USA*
[38]*Perth Exoplanet Survey Telescope, Perth, Western Australia*
[39]*Department of Astronomy, The University of Texas at Austin, 2515 Speedway, Stop C1400 Austin, TX 78712-1205, USA*

This paper has been typeset from a TEX/LATEX file prepared by the author.

Downloaded from https://academic.oup.com/mnras/article/493/1/973/5717324 by guest on 13 May 2022